ChemPhotoChem

Chemistry Europe
European Chemical Societies Publishing
ChemPhotoChem

RESEARCH ARTICLE OPEN ACCESS

Freezing Out Vavilov's Rule: Temperature-Dependent Fluorescence of a Rhodanine Dye

Ottavia Racchi[1] | Stefano Scurti[2] | Stefano Liotino[2] | Andrea Lanfranchi[3] | Anna Painelli[1] | Davide Comoretto[3] | Nađa Došlić[4] | Daniele Caretti[2] | Cristina Sissa[1]

[1]Department of Chemistry, Life Sciences and Environmental Sustainability, University of Parma, Parma, Italy | [2]Department of Industrial Chemistry "Toso Montanari", Bologna, Italy | [3]Department of Chemistry and Industrial Chemistry-DCCI, Genova, Italy | [4]Department of Physical Chemistry, Ruder Bošković Institute, Zagreb, Croatia

Correspondence: Cristina Sissa (cristina.sissa@unipr.it)

Received: 5 August 2025 | **Revised:** 21 November 2025 | **Accepted:** 28 November 2025

Keywords: near-degenerate nπ*-ππ* excited states | rhodanine dyes | temperature dependent fluorescence | Vavilov's rule

ABSTRACT

This study addresses the anomalous fluorescence of a rhodanine-based organic dye of interest for nonlinear optical applications. At room temperature, the dye exhibits weak fluorescence, while spectra collected in glassy 2Me-THF at 77 K show a surprising fluorescence intensity increase by several orders of magnitude with respect to room temperature. Moreover, a pronounced dependence of the fluorescence quantum yield on the excitation wavelength is observed, indicating a breakdown of Vavilov's rule, a corollary of Kasha's rule, which states that the fluorescence quantum yield is independent of the excitation energy. Quantum chemical calculations demonstrate the presence of a bright ππ* excited state that lies very close in energy to a dark nπ* state. The subtle interplay between these two excited states with different natures is responsible for the intriguing spectral behavior of the dye. Specifically, experimental results are rationalized in terms of a population branching between the two excited states, which can be tuned upon varying the temperature or the excitation energy.

1 | Introduction

The lowest electronically excited states, and more specifically the lowest singlet excited state (S_1) and the lowest triplet excited state (T_1), usually determine the photophysics and photochemistry of molecular materials. Kasha's rule establishes the connection between excitation and emission processes, asserting that in any condensed phase, significant photon emission (fluorescence or phosphorescence) only occurs from the lowest excited state of a given multiplicity (singlet or triplet), regardless of the initial photoexcited state [1, 2]. A corollary to the Kasha's rule, known as Vavilov's rule, posits that "the quantum yield of luminescence remains constant regardless of the wavelength of the excitation light" [3]. Kasha's rule is an empirical principle relying on the fast relaxation of an excited molecule toward the lowest excited state in the same spin manifold. This internal conversion typically occurs in a few hundreds of femtoseconds. Consequently, emission (which typically occurs in the nanosecond time window) is only observed from the lowest excited state, the so-called Kasha state. Although not exact laws, the Kasha and Vavilov rules are generally valid, with few noteworthy exceptions that deserve attention to shed light on the mechanisms of excited-state relaxations [4, 5]. Non-Kasha behavior was first observed in the azulene molecule, which emits from the second excited state S_2 [6–8]. Striking but rare deviations from Kasha's rule are observed with dual fluorescence, in systems where emissions come from a high-energy singlet state with an unusually long lifetime as well as from the conventional Kasha state [4, 8]. Some of us recently reported an intriguing case of a false violation of the Kasha's rule in multibranched phenyleneethynylenes, which was attributed to symmetry breaking in the excited state

Ottavia Racchi and Stefano Scurti contributed equally to this work.

[9]. In the literature, only a few systems violating Vavilov rule are reported, and there is great interest in these systems since their photophysical properties are highly interesting from an applicative perspective and are not easily predictable [10–13]. Specifically, anti-Kasha behavior is of special interest in photochemistry, as it opens the possibility to affect the reaction pathway by changing the excitation wavelength.

In this work, we report a joint experimental and theoretical investigation of a rhodanine-based dye initially proposed by Chandrasekharan et al. for applications in nonlinear optics, further functionalized with a methacrylic residue to develop a polymerizable dye [14] (compound **7**, Figure 1). The results obtained by Chandrasekharan et al. are impressive and inspired us to use this dye in organic photonic devices [15]. However, the electronic properties and the role of the thioaxothiazolidine residue were not investigated. A detailed spectroscopic analysis of the molecule in different solvents and over a range of temperatures, supported by computational results, reveals a novel photophysical process that implies a violation of Vavilov's rule, arising from the presence of two excited states that lie very close in energy but are qualitatively different in nature, one being almost dark and the other bright. The observed behavior is in line with results obtained for completely different molecular systems, having nπ* and ππ* states lying very close in energy [16–18]. These results have been interpreted in terms of vibronic interaction between close-lying nπ* and ππ*, a phenomenon that has been named the "proximity effect" [19, 20].

2 | Results and Discussion

2.1 | Synthesis and Characterization of Rhodanine-Based Dye

A multistep synthetic strategy was developed to prepare a novel rhodanine-based dye, with the reaction pathway depicted in Figure 1. The structure consists of an aromatic heterocyclic acceptor system in which imidazole-thiadiazole groups are fused together and substituted by phenyl and thiophene donor groups. The imidazo[2,1-b][1,3,4]thiadiazole core was further functionalized with a rhodanine residue by Vilsmaier reaction to obtain the compound **5**. Although the synthetic route to prepare **5** was previously reported by Kakekochi et al. [15], an optimization process was undertaken to improve the yield and reduce the complexity of purification steps of each reaction. Subsequently, the methacrylic dye (**7**) was prepared via a substitution reaction using hydroxyethyl methacrylate (HEMA) as the polymerizable double-bond moiety. Each intermediate was characterized using a combination of 1H-NMR, 13C-NMR, 2D-NMR experiments, and Fourier transform infrared (FTIR) spectroscopy. The acquired spectra are reported in the Supplementary Information (SI) (see Figures S1–S6, Supporting Information).

2.2 | Room-Temperature Spectroscopy: Probing the Presence of a Low-Energy Dark State

UV–vis absorbance and emission spectra of **7** in solvents of different polarity, toluene, dichloromethane (DCM) and dimethylsulfoxide (DMSO) collected at room temperature are shown in Figure 2a, with main features summarized in Table 1. Absorbance spectra of **7** are insensitive to solvent polarity, while a marginal positive solvatochromism is observed in emission, indicating a negligible effect of the dielectric environment (solvent polarity). Emission intensity is very weak, with a fluorescence quantum yield of ≈0.1% in toluene (Table 1). The lifetime (Table S1, Figure S7, Supporting Information) shows a biexponential decay, with both components on the nanosecond timescale, unambiguously excluding that the observed emission process is related to phosphorescence and then to triplet states. The observed weak emissivity suggests the presence of an optically forbidden (dark) excited state. Two-photon absorption (TPA) is a convenient nonlinear spectroscopic technique to investigate dark states. Indeed, the intensities of the one-photon absorption (OPA) and TPA bands are governed by different rules that, in centrosymmetric systems, lead to the mutual exclusion rule, and, in a nonsymmetric molecule like the investigated dye, can make states hardly visible in OPA well evident in TPA. The TPA spectrum was collected in DCM (Figure 2b) exploiting the two-photon excitation fluorescence technique, described in the Experimental Section. The TPA spectrum shows a shoulder in the 475–525 nm spectral region that is not present in the linear absorption spectrum. This shoulder is safely ascribed to a low-energy dark state that, while poorly emissive, contributes to the nonlinear optical responses of the system [14, 15]. The noncoincidence of OPA and TPA spectra was also clearly confirmed in EtOH (Figure S9, Supporting Information),

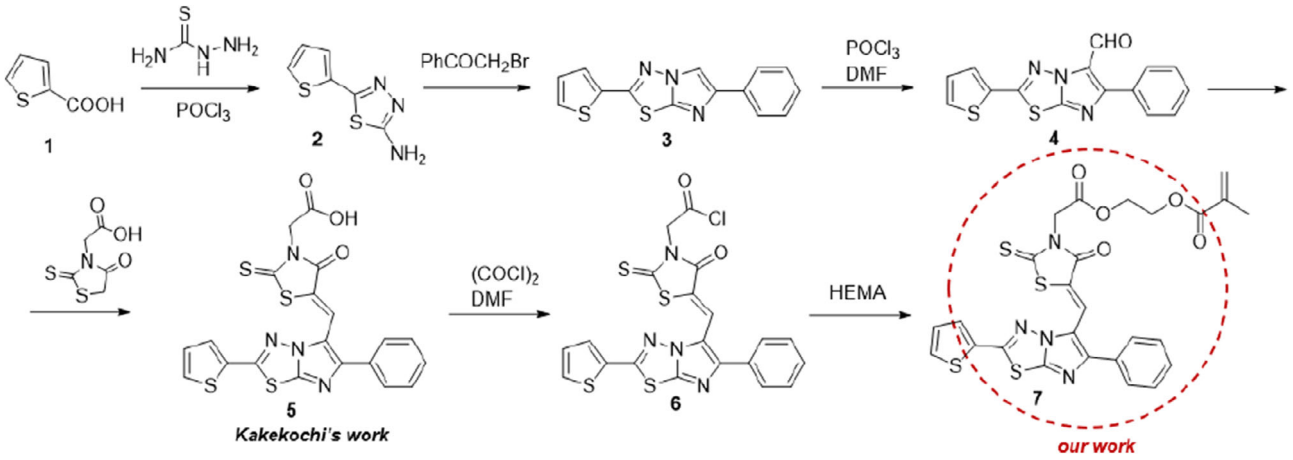

FIGURE 1 | Reaction pathway for dye **7**.

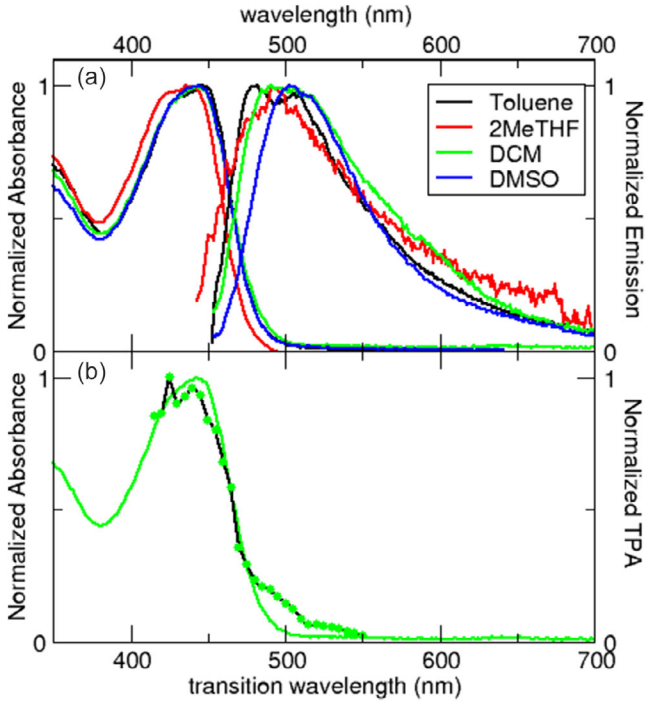

FIGURE 2 | Spectroscopic characterization of **7** at room temperature. (a) Absorbance and emission spectra of **7** in solvents of different polarity. Emission spectra were collected exciting at the absorbance maximum. Emission spectra were modified by subtracting Raman peaks (raw emission spectra are reported in Figure S8, Supporting Information); (b) one-photon absorption (green line) and two-photon absorption spectra (dots) of **7** in DCM.

supporting the conclusion that solvent polarity plays a negligible role.

2.3 | Computational Analysis

All quantum chemical calculations are run in gas phase. Indeed, as observed in previous section, polar solvation has marginal spectroscopic effects. On the other hand, the proper handling of electronic solvation (as related to the solvent refractive index) is delicate and hardly captured in available computational approaches [21, 22].

MP2/cc-pVDZ optimization yields a minimum where the rhodanine fragment is rotated by 40° relative to the imidazo[2,1-b][1,3,4] thiadiazole core (Z stereoisomer). Vertical excitation energies were calculated using the algebraic diagrammatic construction to second order (ADC(2))-cc-pVDZ from the MP2 minimum. Table 2 and Figure 3 summarize key results. The first excited state (S_1) is bright (oscillator strength = 0.508) and corresponds to a delocalized $\pi \rightarrow \pi^*$ transition (see natural transition orbitals (NTOs) in Figure 3a). The second excited state, only 0.1 eV higher in energy, has $n\pi^*$ character and is localized on the rhodanine C=S group (Figure 3b). The two states are in thermodynamic equilibrium, and the ratio of their populations can be calculated using the Boltzmann distribution. For an energy gap of 0.1 eV, the population of the second excited state (the dark state) is negligible at room temperature. Inclusion of diffuse functions at the ADC(2)/aug-cc-pVDZ//MP2/cc-pVDZ level does not affect the ordering of the states. The $S_1(\pi\pi^*)$ state is found at 2.85 eV and the $S_2(n\pi^*)$ state at 3.02 eV above the ground state. The energy

TABLE 2 | ADC(2)/cc-pVDZ vertical excitation energies (in eV) and oscillator strengths (in parentheses) computed at the ground-state minimum geometry (S_0^{min}) and at the S_1 minima of the $\pi\pi^*$ and $n\pi^*$ states.

State	$E(S_0^{min})$	$E(S_1^{min}(\pi\pi^*))$	$\Delta E(S_1^{min}(n\pi^*))$
S_1	2.99 (0.508)	2.54 (0.499)	1.88 (0.010)
S_2	3.09 (0.013)	2.87 (0.012)	2.39 (0.436)
S_3	3.69 (0.262)	3.39 (0.161)	3.18 (0.065)
S_4	3.90 (0.125)	3.72 (0.150)	3.55 (0.081)

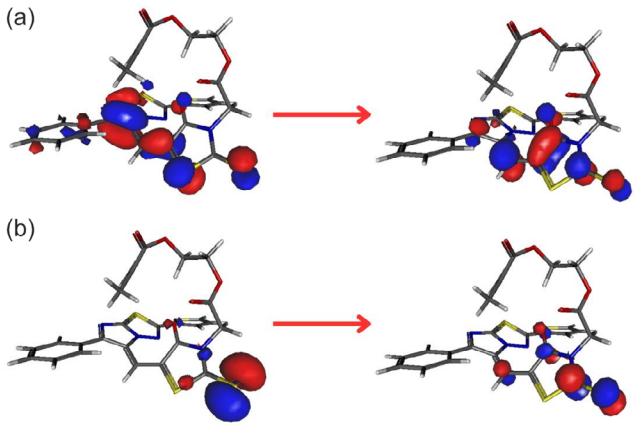

FIGURE 3 | Dominant NTO pairs of **7** for the (a) first transition and (b) the second transition computed at the MP2 optimized ground state geometry.

TABLE 1 | Spectroscopic data of **7** in different solvents, collected at room temperature.

Solvent	Refractive index	Dielectric constant	λ_{max}^{abs} (nm)	Molar extinction coefficient (M^{-1} cm^{-1})	λ_{max}^{em} (nm)	Stokes shift[a] (cm^{-1})	Emission quantum yield (%)
Toluene	1.497	2.38	447	—	482	1624	0.1
2MeTHF	1.408	6.97	436	—	491	2569	—
DCM	1.424	8.93	443	—	491	2207	—
DMSO	1.478	46.7	444	2.26×10^4	503	2642	—

[a]The Stokes shift is calculated as the energy difference between the maxima of absorption and emission spectra.

difference of 0.17 eV is slightly larger than the one at the ADC(2)/cc-pVDZ level. Higher-energy states are too far away (Table 2) and they are not relevant to the discussion. We have also investigated the E stereoisomer obtained by rotating the imidazole-thiadiazole unit around the C═C axis. The MP2/cc-pVDZ optimized minimum energy structure of the E stereoisomer (for the Cartesian coordinates see Supporting Inforamtion) is 1.13 kcal/mol higher in energy than the Z stereoisomer, that we have investigated in detail. At room temperature the Z:E ratio is 87:13. As for the Z stereoisomer, the first excited state (S_1) of the E stereoisomer has ππ* character and lies 2.93 eV above the ground state, and second excited state (S_2) has nπ* character and is found at 3.09 eV.

The energy gap and the relative order of the two excited states of interest are highly sensitive to dye geometry and to the adopted computational method. Notably, TD-DFT predicts the opposite state order (see Tables S2 and S3, Supporting Information). Indeed, the small energy gap between the two states is comparable to the accuracy of computational methods [23, 24]. Regardless of the specific order of the two states and of the precise magnitude of the relevant energy gap, computational results are in line with experimental data that confirm the presence of a dark state lying close in energy to the bright state responsible for the strong absorption band. The computed transition energy, calculated in ADC(2) at 2.99 eV (415 nm), is slightly overestimated versus experiment, as expected, since neither zero-point energy contributions nor environmental effects are accounted for.

Fluorescence is a vertical process from the relaxed excited state. To investigate emission, we optimized the geometries of the first excited state at the ADC(2)/cc-pVDZ level of theoryand relevant results are summarized in Table 2. Optimization of S_1(ππ*) yields a bright minimum at 2.54 eV above the ground state. The dominant NTO pairs are shown in the Supporting Information (see Figure S10b). Optimization of S_2 (nπ*) leads to a conical intersection (CI) with S_1 (ππ*). Extrapolation beyond the CI region results in a second minimum on the adiabatic S_1 surface, denoted S_1 (nπ*), which is dark and located 1.88 eV above the ground state (for the corresponding NTO see Figure S10a, Supporting Information).

The potential energy profile of the dye can be better understood by examining the reaction pathways connecting the Franck–Condon (FC) geometry to the relevant excited-state minima. Figure 4 presents two linearly interpolated reaction paths (LIP) connecting the FC geometry (vertical line) with the S_1 (ππ*) minimum (right) and the S_1 (nπ*) minimum (left). The diabatic ππ* and nπ* states are shown in red and blue, respectively.

The path toward the S_1(ππ*) minimum is barrierless and involves an increase in the C═S bond length from 1.64 to 1.67 Å and the C═C bond length from 1.37 to 1.42 Å. The path from the S_1(ππ*) state at the FC geometry toward the S_1(nπ*) minimum involves crossing the S_2 (nπ*)/S_1(ππ*) CI seam, with a small barrier of 0.04 eV. Given the limitations of electronic structure methods, the precise determination of the height of such a small barrier is hardly possible. In summary, the weak emission observed at room temperature is ascribed to the presence of a dark (nπ*) state lying energetically close to the bright (ππ*) state, as confirmed by TPA data and supported by high-quality computational results. The nanosecond biexponential decay may originate from the presence of conformational disorder, due to the flexibility of the molecule, and/or by a partial population of both excited the nπ* and ππ* states, each contributing to the overall emission. The

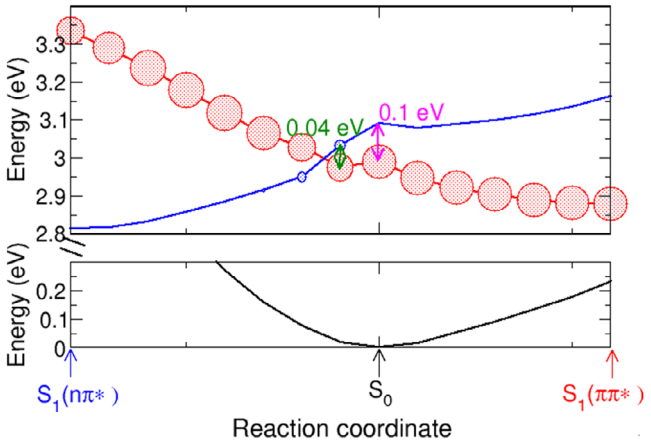

FIGURE 4 | Potential energy profiles of the ground state (black) and of two lowest excited states S_1 (ππ*) (red), S_2 (nπ*) (blue). Circles represent the oscillator strengths of the transition from the ground state. Blue, black and red arrows on the bottom indicate the equilibrium geometry of S_1 (ππ*), S_0 and S_1(nπ*) states, respectively. The energy gap between the two states at the FC geometry and the energy barrier at the CI are indicated with magenta and green double arrows, respectively. The energy of the electronic ground state, evaluated at the minima of the S_1(ππ*) and S_1(nπ*) states, is 0.36 and 0.94 eV, respectively, above the ground-state energy at the Franck–Condon geometry.

quasidegeneracy of the two states makes the origin of the observed weak fluorescence hardly ascribable to a single specific state. The dark (nπ*) state, characterized by a very low oscillator strength, could itself be responsible for the weak emission. Alternatively, the bright (ππ*) state may predominantly relax into the dark (nπ*) state at room temperature, but a small residual population in the bright state could still give rise to weak fluorescence [6]. Finally, both states may contribute to the observed emission, a hypothesis that could justify the biexponential decay observed at room temperature. While a definite assignment remains challenging, the collected evidence points toward a complex interplay between quasidegenerate states. In any case, the emission lifetime, in the ns timescale, definitely excludes the involvement of triplet states. Further temperature-dependent spectroscopy studies will provide deeper insight into this behavior.

2.4 | Low-Temperature Spectroscopy: Experimental Evidence of the Breakdown of Vavilov's Rule

To further investigate the excited state landscape of **7**, low-temperature spectroscopic measurements were conducted in 2Me-THF. When rapidly cooled, 2Me-THF undergoes a glass transition at 103 K [25], enabling the measurement of optical spectra in a solid matrix at low temperature with minimal detrimental light scattering effects. Absorbance spectra (Figure 5a) show the emergence of well-resolved vibronic transitions, due to reduced inhomogeneous broadening, that also induces an increase of the peak absorbance as temperature decreases, due to the narrower bandwidth. The most surprising effects are observed in emission spectra (Figure 5b) with a huge increase of the emission intensity below 195 K. This emission, with a lifetime of ≈2 ns (Figure 2c and Table S1, Supporting Information), is safely ascribed to a fluorescence process.

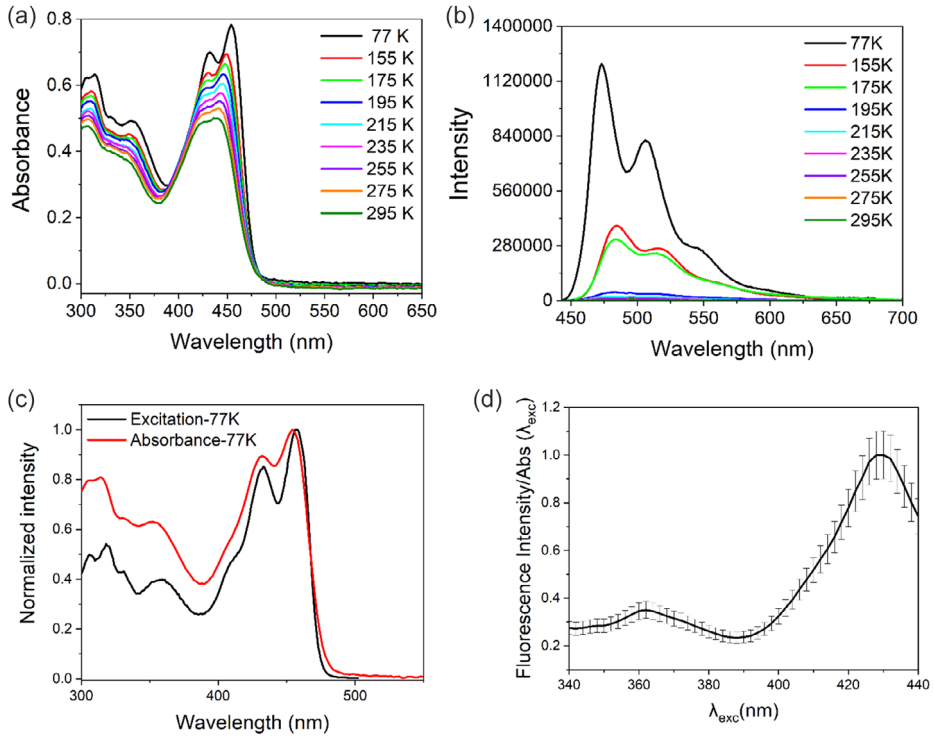

FIGURE 5 | (a) Absorbance spectra as a function of temperature of dye **7** in 2Me-THF; (b) emission spectra as a function of temperature of dye **7** in 2Me-THF; note that from 295 to 155 K for emission spectra slits were open at 2 nm, while at 77 K slits were set at 1 nm to avoid detector saturation; (c) comparison between the excitation and absorbance spectra of the dye measured in 2Me-THF at 77 K; (d) excitation wavelength dependence of a quantity proportional to the fluorescence quantum yield (ratio between the integrated fluorescence intensity and the absorbance at the excitation wavelength). The ratio refers to experimental data collected at 77 K. Error bar: ± 10%.

Interestingly, the fluorescence excitation spectrum measured at 77 K differs significantly from the absorption spectrum, as shown in Figure 5c: upon normalization of both spectra at their maxima (λ_{max}), the excitation spectrum is always weaker with respect to the absorption spectrum for wavelength shorter than λ_{max}. The qualitatively different profile of the excitation spectrum versus the absorption spectrum suggests that the fluorescence quantum yield acquires a dependence on the excitation wavelength, thereby violating Vavilov rule. Figure 5d shows the dependence on the excitation wavelength of the integrated emission intensity divided by the absorbance at the excitation wavelength. This quantity, proportional to the fluorescence quantum yield, is far from constant in the explored spectral region. Specifically, the fluorescence quantum yield decreases at shorter wavelengths, suggesting that at low temperatures, different decay pathways are accessible upon excitation towards different excited states. For comparison, the same experiments conducted on Nile red, a commercial red emitter, fully confirm Vavilov's rule. As expected, the Nile red excitation spectrum is superimposable with the absorption spectrum at all temperatures, and the ratio between the integrated fluorescence intensity and absorbance at the excitation wavelength marginally varies with the excitation wavelengths (results are shown in Figure S11, Supporting Information).

2.5 | Emission in Thin Films: Effects of Rigidity and Temperature

The anomalous behavior of the investigated compound in glassy 2Me-THF could possibly be related to the rigidity of the medium. To verify this hypothesis, we have collected emission spectra of **7** dispersed in a thin polystyrene film, a method suitable for the preparation of high-quality optical films [26, 27]. The collected emission (Figure S12, Supporting Information) remains very weak at room temperature. The same film cooled down to 77 K shows instead a sizeable increase of the emission intensity (up to ≈10-fold). The temperature-dependent excitation spectra of **7** dispersed in a polystyrene film measured in Figure S13, Supporting Information, show that upon decreasing temperature, the contribution of high-energy states to the observed fluorescence decreases, as observed in liquid solutions. These results unambiguously demonstrate that the amplification of the fluorescence intensity observed at low temperature (Figure 5) is not related to the matrix rigidity, but it is a genuine temperature effect related to the dye properties.

3 | Discussion

The unusual very large increase of the fluorescence intensity observed for **7** at low temperature is unambiguously assigned to a purely thermal effect. Importantly, in our system the emission lifetime remains constant with temperature, indicating that the radiative rate does not change and that the intensity increase originates from the suppression of thermally activated nonradiative decay. Analogous decoupling between intensity and lifetime has been reported, for example, in systems where thermal trapping processes control the emission efficiency [28]. Computational results indicate the presence of two excited states of different nature, that are very close in energy: the dark nπ* state lies only

0.1 eV above the bright first excited ππ* state, while the energy barrier is of the order of 0.04 eV. The thermal energy available at room temperature is ≈0.026 eV (0.6 kcal/mol) and decreases to 0.01 eV (0.25 kcal/mol) at 77 K. Thus, even such a tiny barrier can hinder population transfer from the initially excited bright ππ* state to the dark nπ* state at low temperature. The presence of the dark, low-energy excited state is supported by nonlinear experimental spectra: TPA spectra in two solvents show a weak shoulder at longer wavelengths compared to linear absorption spectra. The exact location of this low-energy, almost dark state from available experimental data is not possible, since only a shoulder is visible, and the maximum of the band lies below the second transition.

Although the ADC(2) method is likely the most reliable electronic structure approach for systems with ≈50 heavy atoms, the associated uncertainties are of the same order of magnitude as the estimated energy gap [23, 24], and a definite statement about the actual ordering of the electronic states is impossible. However, the ordering of states offered by ADC(2)/cc-pVDZ allows for a plausible interpretation of the observed experimental results. At room temperature, following excitation to the bright state (top panel of Figure 6; vertical excitation is depicted with a vertical black arrow), the system has sufficient energy to cross the barrier to the $S_2(n\pi^*)/S_1(\pi\pi^*)$ CI, allowing partial population transfer to the nπ* state. The remaining population stays in the bright state and decays toward the $S_1(\pi\pi^*)$ minimum. Branching the population between the two states makes the system poorly emissive. When exciting at higher energy, the branching of population still occurs but possibly with different ratios, as suggested by the absence of superposition between excitation and absorbance spectra, as reported in Figure S14, Supporting Information. However, the system remains poorly emissive, hindering the possibility of measuring the wavelength dependence of the fluorescence quantum yield.

At low temperature (central and bottom panel of Figure 6), a strong increase of fluorescence intensity is observed. The change in fluorescence intensity is also accompanied by a mismatch between the excitation and the absorbance spectrum and an impressive dependence of the fluorescence quantum yield on the wavelength, a manifest breakdown of Vailov's rule. After excitation at low energy, the $S_2(n\pi^*)/S_1(\pi\pi^*)$ CI is no longer accessible, and the system remains in the bright state and radiatively relaxes to the ground state via fluorescence emission. However, when the system is excited to higher excited states (bottom panel of Figure 6), it has enough energy to overcome the barrier, and the excited state population decays toward both the dark state and the bright state, resulting in an overall suppression of the fluorescence quantum yield upon excitation at shorter wavelengths.

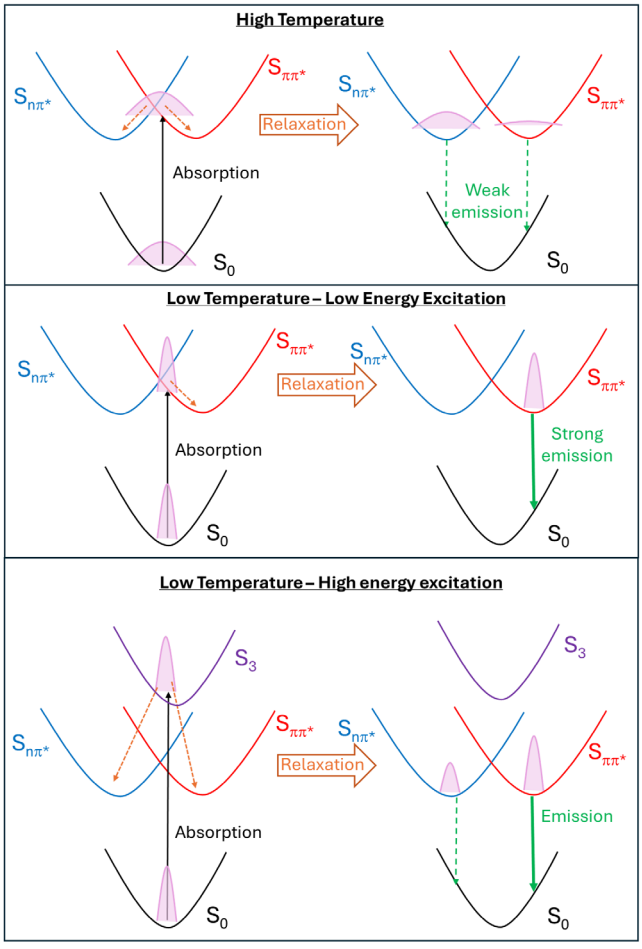

FIGURE 6 | Schematic representation of the spectroscopic behavior of dye **7**.

4 | Conclusion

In this article, we present a comprehensive spectroscopic analysis of a rhodanine-based dye (**7**), synthesized starting from the work in Ref. [15]. We demonstrated that, by lowering temperature, the fluorescence intensity of the system increases by approximately two orders of magnitude. This behavior is ascribed to the tuning of the relative populations of two quasidegenerate states characterized by very different radiative rates. The relaxation pathway and hence the complex photophysics of the investigated system are determined by a subtle interplay between internal conversion and vibronic coupling. Operative parameters, including temperature and excitation energy, then crucially affect the relative population of the quasidegenerate states, therefore defining the dominant emissive channel. Through detailed spectroscopic characterization of the dye in different environments and at different temperatures, we were able to unambiguously assign the unusually very large increase of the fluorescence intensity observed at low temperature to a purely thermal effect. We have experimentally demonstrated the breakdown of the Vavilov's rule at low temperature for the rhodanine-based dye (**7**), and we have proposed a plausible mechanism to explain the observed results, based on temperature-dependent relaxation paths. This mechanism could virtually occur in other systems having low-energy excited states that are very close in energy but with different oscillator strengths (one of them being almost dark). The work also elucidates the presence of multiple excited states in the investigated compound that can potentially contribute to optical nonlinearities, as already investigated in the work of Puthiya Purayil et al. [14]. Moreover, this work also suggests that electronic properties of dyes should be carefully checked when temperature-dependent measurements are performed, since temperature could deeply affect de-excitation paths.

5 | Experimental

5.1 | Synthesis and Structural Characterization of Rhodanine-Based Dye

Synthetic methodologies for the preparation of rhodanine-based dye, along with their structural characterizations (NMR, 2D-NMR, FTIR), are reported in the Supporting Information (SI). Each intermediate was characterized by a combination of 1H-NMR, 13C-NMR, and 2D-NMR spectroscopy by using a Bruker Avance 600, operating at 600 MHz. Deuterated DMSO (d_6-DMSO) was used as an NMR solvent and TMS as an internal reference standard. The compounds were also characterized by FTIR, the spectra were recorded through an ATR-IR Bruker Alpha I spectrometer.

5.2 | Linear Spectroscopic Characterization

UV–vis absorbance spectra were recorded using a PerkinElmer Lambda 650 spectrophotometer. Fluorescence spectra were measured employing a FLS1000 Edinburgh Fluorimeter, equipped with a 450 W Xenon Lamp and a PMT-900 Detector, exciting the sample at the maximum of its absorbance. Excitation spectra were collected, detecting the intensity on the maximum of the emission spectrum. Excitation and emission spectra were corrected for excitation intensity (monitored with a dedicated calibrated detector) and detector sensitivity, respectively. These corrections ensure that the spectral shapes obtained with different spectrometers can be reliably compared. Toluene (Sigma-Aldrich, purity ≥ 99.5%), DCM (Carlo Erba, purity ≥ 99.8%), DMSO (Sigma-Aldrich, purity ≥ 99.7%), and 2-methyltetrahydrofuran (2Me-THF, Sigma-Aldrich, purity ≥ 99.5%) were utilized to prepare the solutions. In order to avoid inner filter effects in fluorescence spectra, solutions were prepared with absorbance <0.1. Absorbance spectra were acquired on solutions with absorbance between 0.5 and 1. Absorbance and fluorescence spectra were acquired using a quartz cuvette with an optical path length of 1 cm.

The fluorescence quantum yield was determined versus fluorescein dissolved in a 0.1 M NaOH solution as reference ($\Phi_f = 0.92$ [29]).

Lifetime decay measurements of the dye in DCM and 2-Me-THF were measured upon excitation of the sample with a picosecond pulsed diode laser at 405 nm (pulse width < 100 ps) and collecting emission at 500 nm. The fitting of the decay lifetimes collected at room temperature was performed by accounting for the instrument response function (IRF). For the fitting of the lifetime collected at low temperature, the IRF was neglected.

5.3 | Low-Temperature Spectroscopic Characterization

Emission and absorbance spectra as a function of temperature were measured using the FLS1000 Edinburgh Fluorimeter described before and a silicon photodiode mounted within the sample chamber to monitor the changes in the intensity of the excitation beam due to absorption.

The solutions, prepared with 2-Me-THF (Sigma-Aldrich, purity ≥ 99.5%, stored for one night under molecular sieves and filtered), were cooled using an Oxford Instruments OptistatDN cryostat, which provided a controlled low-temperature exchange gas environment for the samples held in cryogenic quartz cuvettes. The 2Me-THF solutions were rapidly cooled to 77 K to obtain a transparent glass. Under these conditions, the motion of solute molecules during the excited-state lifetime can be safely neglected. The temperature of the sample was then incrementally raised to 155, 175, 195, 215, 235, 255, 275, and 295 K.

The samples for the absorption spectra measurements were prepared with an absorbance of ≈0.5 at room temperature. For acquiring the emission spectra, the sample was diluted to have an absorbance <0.1.

5.4 | Two-Photon Excited Fluorescence

Two-photon absorption (TPA) spectra were obtained by means of the two-photon excited fluorescence technique. Two-photon excitation spectra were collected with a Nikon A1R MP+ multiphoton upright microscope. A tunable femtosecond mode-locked laser (Coherent Chameleon Discovery) spanning wavelengths from 660 to 1320 nm served as the radiation source. A water-dipping objective (25x, NA = 1.1) was utilized to focus the excitation beam and collect the resulting TPEF signal. Detection of the TPEF signal was achieved through three non-descanned detectors (NDDs) covering blue (415–485 nm), green (506–593 nm), and red (604–679 nm) ranges, along with a spectral detector connected to the microscope via an optical fiber. TPA spectra were recorded in DCM solution and ethanol (Sigma-Aldrich, purity ≥ 99.8%).

Liquid samples were examined in quartz cuvettes positioned horizontally under the microscope objective. Each cuvette was entirely filled with the liquid sample to eliminate air gaps between the upper wall and the solution. Distilled water was used to ensure proper contact between the objective and the cuvette. During each measurement, the excitation beam was focused as close as possible to the cuvette's upper wall to mitigate artifacts arising from differences in solvent refractive indices and inner-filter effects.

5.5 | Computational Analysis

The geometry of the investigated dye was optimized using the Turbomole 7.8 package [30] at the MP2/cc-pVDZ level of theory [31], employing the resolution-of-identity (RI) approximation [32].

Vertical excitation energies and oscillator strengths were computed using second-order algebraic-diagrammatic construction (ADC(2)) method [33,34], as implemented in Turbomole 7.8 [30]. Calculations were performed with cc-pVDZ basis sets and aug-cc-pVDZ basis sets.

Excited states were characterized using natural transition orbitals (NTOs) [36, 37], computed by retaining only singly excited coefficients of the ADC(2) wave functions [38] employing an in-house software.

Two minima with distinct electronic characters were optimized on the first excited state (S_1) with ADC(2)/cc-pVDZ. These minima and the FC geometry were connected in a linearly interpolated reaction path (LIP). LIPs were computed by converting the initial (FC) and final geometries ($S_1^{min}(\pi\pi^*)$) and ($S_1^{min}(n\pi^*)$) to internal coordinates, ensuring consistent atom ordering. The difference between the two sets of internal coordinates was then

calculated, and nine interpolation points were generated by linearly interpolating each internal coordinate. The resulting geometries were subsequently transformed back to Cartesian coordinates, and ADC(2) vertical excitation energies were computed at these geometries to obtain the LIPs. In total, 17 geometry points were used to connect the nπ* and ππ* minima via the FC geometry. The Cartesian coordinates of all relevant structures are provided in the Supporting Information. The energy difference between the two lowest excited states at the FC geometry is below the ADC(2) mean absolute error of 0.2–0.3 eV [35]. To assess the robustness of these results, DFT and TD-DFT calculations were carried out using the Coulomb-attenuated hybrid functional CAM-B3LYP, as well as B3LYP and M06-2X, in combination with the polarized split-valence 6-31G(d) basis set using Gaussian software. Ground state optimized geometry at the DFT level.

Excited state calculations were carried out using the same basis set and functional applied for geometry optimization. DFT and TD-DFT optimized geometries and vertical excitation energies are given in the Supporting Information.

5.6 | Thin Film Preparation

Thin films of dye embedded in a polymeric matrix were solution-processed via the spin-coating technique. A solution of polystyrene (Aldrich, $M_w = 192{,}000$) in chloroform was prepared with 30 mg ml^{-1} concentration. The solution was used to dissolve the dye with a concentration of 1 mg ml^{-1}. 150 µl of the final solution were then spin-cast at a rotational speed of 6000 rpm on an air plasma cleaned, 1 mm-thick glass substrate sized 2.5×2.5 cm^2 to form a thin film of good optical quality [39].

Acknowledgments

O.R. position was funded by PNRR MUR project ECS-00000033-ECOSISTER. C.S. and A.P. were financially supported by PNRR MUR project PE0000023-NQSTI. O.R., C.S. and A.P. acknowledge the support from the local HPC (High Performance Computing) facility and from the equipment and framework of the COMP-R Initiative, funded by the "Departments of Excellence program of the Italian Ministry for University and Research" (MUR, 2023–2027). N.D. acknowledges the support of the Croatian Science Foundation under the project number [HRZZ-IP-2022-10-4658]. Work in Bologna and Genova is supported by PRIN MUR project 2020TS9LXS Polymer mETamateriALs for nanophotonicS (PETALS). S.S. position was funded by FSE+ 2021–2027 (RIF. PA: 2023-20090/RER-2-CUP: J19J23000730002).

Conflicts of Interest

The authors declare no conflicts of interest.

References

1. M. Kasha, "Characterization of Electronic Transitions in Complex Molecules," *Discussions of the Faraday Society* 9 (1950): 14.

2. M. Kasha and S. McGlynn, "Molecular Electronic Spectroscopy," *Annual Review of Physical Chemistry* 7 (1956): 403.

3. V. Gold, in *The IUPAC Compendium of Chemical Terminology*, International Union of Pure and Applied Chemistry (IUPAC), (Research Triangle Park, NC 2019).

4. A. P. Demchenko, V. I. Tomin, and P.-T. Chou, "Breaking the Kasha Rule for More Efficient Photochemistry," *Chemical Reviews* 117 (2017): 13353.

5. K. Veys and D. Escudero, "Anti-Kasha Fluorescence in Molecular Entities: Central Role of Electron–Vibrational Coupling," *Accounts of Chemical Research* 55 (2022): 2698.

6. E. Campioli, S. Sanyal, A. Marcelli, et al., "Addressing Charge-Transfer and Locally-Excited States in a Twisted Biphenyl Push-Pull Chromophore," *ChemPhysChem* 20 (2019): 2860.

7. D. Dunlop, L. Ludvíková, A. Banerjee, H. Ottosson, and T. Slanina, "Excited-State (Anti)Aromaticity Explains Why Azulene Disobeys Kasha's Rule," *Journal of the American Chemical Society* 145 (2023): 13974.

8. B. H. Jhun, D. Y. Jeong, S. Nah, S. Y. Park, and Y. You, "Novel Anti-Kasha Fluorophores Exhibiting Dual Emission with Thermally Activated Delayed Fluorescence through Detouring Triplet Manifolds," *Journal of Materials Chemistry C* 9 (2021): 7083.

9. K. Swathi, M. Sujith, P. S. Divya, et al., "From Symmetry Breaking to Symmetry Swapping: Is Kasha's Rule Violated in Multibranched Phenyleneethynylenes?" *Chemical Science* 14 (2023): 1986.

10. K. E. Henry, R. G. Balasingham, A. R. Vortherms, et al., "Emission Wavelength Variation with Changes in Excitation in a Re(I)–Bisthiazole Ligand Complex That Breaks the Kasha–Vavilov Rule," *Chemical Science* 4 (2013): 2490.

11. O. Yushchenko, G. Licari, S. Mosquera-Vazquez, N. Sakai, S. Matile, and E. Vauthey, "Ultrafast Intersystem-Crossing Dynamics and Breakdown of the Kasha–Vavilov's Rule of Naphthalenediimides," *The Journal of Physical Chemistry Letters* 6 (2015): 2096.

12. Z. Hou, J. Guan, J. Peng, X. Li, Z. Yu, and J. Zheng, "Double Crossing Conical Intersections and Anti-Vavilov Fluorescence in Tetraphenyl Ethylene," *The Journal of Chemical Physics* 156 (2022): 144302.

13. P. A. Tarakanov, A. V. Kozlov, A. O. Simakov, N. S. Goryachev, and V. E. Pushkarev, "Breakdown of the Kasha–Vavilov's Rule in Low-Symmetry Porphyrazines: Ultrafast Intersystem Crossing via High Vibronic State," *Photochemistry and Photobiology* 101 (2025): 1402.

14. N. Puthiya Purayil, V. Kakekochi, U. K. Dalimba, and K. Chandrasekharan, "All-Optical Diode Action through Enhanced Nonlinear Response from Polymeric Photonic Crystal Microcavity," *ACS Applied Electronic Materials* 4 (2022): 138.

15. V. Kakekochi, U. D. Kumar, and K. Chandrasekharan, "Effects of Substituents on the Enrichment of the Optical Limiting Action of Novel Imidazo[2,1-b]-[1,3,4]thiadiazole Fused Thiophene-Based Small Molecules," *New Journal of Chemistry* 43 (2019): 9232.

16. G. Jiang, J. Liu, and P. Zhou, "Unraveling the Mechanism of ACQ-to-AIE Transformation of Fluorescein Derivatives," *The Journal of Physical Chemistry A* 127 (2023): 5193.

17. Z. Tang and P. Zhou, "Elaborating the Fluorescence Regulation and Quenching Mechanism of Sulfur-for-Oxygen Replacement for Fluorophores," *ChemPhysChem* 25 (2024): e202400503.

18. Z. Tang, P. Li, J. Liu, and P. Zhou, "Carbonyl Stretch as a Franck–Condon Active Mode and Driving Force for Excited-State Decay of 8-Methoxy-4-methyl-2H-benzo[g]chromen-2-one from nπ* State," *The Journal of Physical Chemistry B* 124 (2020): 11472.

19. W. A. Wassam and E. C. Lim, "Proximity Effect in Radiationless Transitions," *The Journal of Chemical Physics* 68 (1978): 433.

20. E. C. Lim, "Proximity Effect in Molecular Photophysics: Dynamical Consequences of Pseudo-Jahn-Teller Interaction," *The Journal of Physical Chemistry* 90 (1986): 6770.

21. D. K. A. Phan Huu, R. Dhali, C. Pieroni, et al., "Antiadiabatic View of Fast Environmental Effects on Optical Spectra," *Physical Review Letters* 124 (2020): 107401.

22. J. M. Kaminski, T. Böhmer, and C. M. Marian, "Balancing TADF Properties in π-Bridged Donor–Acceptor Systems by Sterical

Constraints: The Best of Three Worlds," *The Journal of Physical Chemistry C* 128 (2024): 13711.

23. P.-F. Loos, F. Lipparini, M. Boggio-Pasqua, A. Scemama, and D. Jacquemin, "A Mountaineering Strategy to Excited States: Highly Accurate Energies and Benchmarks for Medium Sized Molecules," *Journal of Chemical Theory and Computation* 16 (2020): 1711.

24. M. Véril, A. Scemama, M. Caffarel, et al., "QUESTDB: A Database of highly Accurate Excitation Energies for the Electronic Structure Community," *Journal of Computational Chemistry* 24 (2024): 1791–1805.

25. M. Mizukami, H. Fujimori, and M. Oguni, "Glass Transitions and the Responsible Molecular Motions in 2-Methyltetrahydrofuran," *Progress of Theoretical and Experimental Physics* 126 (1997) 79–82.

26. L. Magnasco, A. Lanfranchi, M. Martusciello, et al., "Fluorimetric Detection of Vapor Pollutants with Diketopyrrolopyrrole Polymer Microcavities," *ACS Omega* 9 (2024): 42375.

27. H. Megahd, M. Villarreal Brito, A. Lanfranchi, P. Stagnaro, P. Lova, and D. Comoretto, "Control of Near-Infrared Dye Fluorescence Lifetime in All-Polymer Microcavities," *Materials Chemistry Frontiers* 6 (2022): 2413.

28. C. T. Trinh, D. N. Minh, K. J. Ahn, Y. Kang, and K.-G. Lee, "Verification of Type-A and Type-B-HC Blinking Mechanisms of Organic–Inorganic Formamidinium Lead Halide Perovskite Quantum Dots by FLID Measurements," *Scientific Reports* 10 (2020): 2172.

29. D. Magde, R. Wong, and P. G. Seybold, "Fluorescence Quantum Yields and Their Relation to Lifetimes of Rhodamine 6G and Fluorescein in Nine Solvents: Improved Absolute Standards for Quantum Yields," *Photochemistry and Photobiology* 75 (2002): 327.

30. F. Furche, R. Ahlrichs, C. Hättig, W. Klopper, M. Sierka, and F. Weigend, "Turbomole," *WIREs Computational Molecular Science* 4 (2014): 91.

31. T. H. Dunning, "Gaussian Basis Sets for Use in Correlated Molecular Calculations. I. The Atoms Boron through Neon and Hydrogen," *The Journal of Chemical Physics* 90 (1989): 1007.

32. F. Weigend and M. Häser, "RI-MP2: First Derivatives and Global Consistency," *Theoretical Chemistry Acta* 97 (1997): 331.

33. J. Schirmer, "Beyond the Random Phase Approximation: A New Approximation Scheme for the Polarization Propagator," *Physical Review A* 26 (1982): 2395.

34. A. B. Trofimov and J. Schirmer, "An Efficient Polarization Propagator Approach to Valence Electron Excitation Spectra," *Journal of Physics B: Atomic, Molecular and Optical Physics* 28 (1995): 2299.

35. A. Dreuw and M. Wormit, "The Algebraic Diagrammatic Construction Scheme for the Polarization Propagator for the Calculation of Excited States," *WIREs Computational Molecular Science* 5 (2015): 82.

36. R. L. Martin, "Natural Transition Orbitals," *The Journal of Chemical Physics* 118 (2003): 4775.

37. I. Mayer, "Using Singular Value Decomposition for a Compact Presentation and Improved Interpretation of the CIS Wave Functions," *Chemical Physics Letters* 437 (2007): 284.

38. M. Sapunar, T. Piteša, D. Davidović, and N. Došlić, "Highly Efficient Algorithms for CIS Type Excited State Wave Function Overlaps," *Journal of Chemical Theory and Computation* 15 (2019): 3461.

39. A. Lanfranchi, H. Megahd, P. Lova, and D. Comoretto, "Engineering All-polymer Planar Photonic Crystals as Aegises against Sunlight Overheating," *Chemical Engineering Science* 283 (2024): 119377.

Supporting Information

Supporting Information is available from the Wiley Online Library or from the author. **Supporting Fig. S1:** ^{1}H-NMR, ^{13}C-NMR, HSQC, HMBC and FT-IR spectra of **2**. **Supporting Fig. S2:** ^{1}H-NMR, ^{13}C-NMR, COSY, HSQC, HMBC, and FT-IR spectra of **3**. **Supporting Fig. S3:** ^{1}H-NMR and FT-IR spectra of **4**. **Supporting Fig. S4:** ^{1}H-NMR and FT-IR spectra of **5**. **Supporting Fig. S5:** ^{1}H-NMR and FT-IR spectra of **6**. **Supporting Fig. S6:** ^{1}H-NMR and FT-IR spectra of **7**. **Supporting Fig. S7:** Fluorescence decays and Instrument response function (IRF) in DCM at r.T. and 2MeTHF at 77K. **Supporting Fig. S8:** Raw emission spectra of **7**. **Supporting Fig. S9:** One photon absorption and two photon absorption spectra of **7** in ethanol. **Supporting Fig. S10:** a) Dominant NTO of the dark optimized S1($n\pi^*$) b) Dominant NTO of the bright optimized S1($\pi\pi^*$). **Supporting Fig. S11:** Top: comparison between the excitation and absorbance spectra of **7** measured in 2Me-THF at 77K; Bottom: excitation wavelength dependence of a quantity proportional to the fluorescence quantum yield (ratio between the integrated fluorescence intensity and the absorbance at the excitation wavelength). The ratio has been calculated from experimental data collected at 77K. Error bar: ± 10%. Results are not shown in the 400-450nm region because the absorbance signal is too low. **Supporting Fig. S12:** Emission spectra collected from **7** dispersed in a polystyrene thin film at different temperatures. All spectra were collected opening the slits at 2 nm. **Supporting Fig. S13:** Excitation spectra collected from **7** dispersed in polystyrene with a concentration of 1 mg ml^{-1} collected at different temperatures. The opening of the slits for the measurements carried out was 2 nm. **Supporting Fig. S14:** Left panel: comparison between the excitation and absorbance spectra of **7** measured in toluene at 295K. Right panel: qualitative description of the effect of the branching of population. Exciting at high energy, we observe an increment of emission intensity, which is the result of the branching of population, but possibly with different ratios compared to that occurring when exciting at low energy. **Supporting Table S1:** In DCM, the lifetimes were obtained from a reconvolution fit of the fluorescence decays shown in Figure S7, taking into account the instrument response function (IRF). The first ∼2 nanoseconds of the decay were excluded from the fitting procedure, as this portion overlaps significantly with the IRF. Including it would result in artificially short lifetimes, below the time resolution of the instrument. At 77 K, the IRF was not measured under the same experimental conditions as the sample. Nevertheless, a reasonable estimation of the lifetime can still be obtained by excluding the initial nanoseconds of the decay, where the IRF contribution is most significant. As in the case of DCM at room temperature, the first ∼2 nanoseconds were omitted from the fitting. **Supporting Table S2:** Ground state optimized geometry at the DFT level. **Supporting Table S3:** Computational results obtained from TD-DFT/B3LYP/6-31g(d) and TD-DFT/M062X/6- 31g(d) calculations in gas phase.